Surfactant-like peptide self-assembled into hybrid nanostructures for electronic nose applications

Jonathan Weerakkody, Marielle El Kazzy, Elise Jacquier, Pierre-Henri Elchinger, Raphael Mathey, Wai Li Ling, Cyril Herrier, Thierry Livache, Arnaud Buhot, Yanxia Hou

Surfactant-like Peptide Self-assembled into Hybrid Nanostructures for Electronic Nose Applications

Jonathan S. Weerakkody,[†] Marielle El Kazzy,[†] Elise Jacquier,[†] Pierre-Henri Elchinger,[†] Raphael Mathey,[†] Wai Li Ling,[‡] Cyril Herrier,[¶] Thierry Livache,[¶] Arnaud Buhot,[†] and Yanxia Hou*[,†]

†*Univ. Grenoble Alpes, CEA, CNRS, IRIG, SyMMES, 17 Rue des Martyrs, Grenoble 38000, France*

‡*Univ. Grenoble Alpes, CEA, CNRS, IRIG, IBS, 71 Avenue des Martyrs, Grenoble 38000, France*

¶*Aryballe, 7 Rue des Arts et Métiers, Grenoble 38000, France*

E-mail: yanxia.hou-broutin@cea.fr

Abstract

An electronic nose (e-nose) utilizes a multi-sensor array, which relies on the vector contrast of combinatorial responses, to effectively discriminate between volatile organic compounds (VOCs). In recent years, hierarchical structures made of non-biological materials have been used to achieve the required sensor diversity. With the advent of self-assembling peptides, the ability to tune nanostructuration, surprisingly, has not been exploited for sensor array diversification. In this work, a novel designer surfactant-like peptide (SLP) sequence $CG_7{-}NH_2$ is used to fabricate morphologically and physicochemically heterogeneous 'biohybrid' surfaces on Au-covered chip. For the

first time, multi-structural surfaces containing immobilized hierarchical nanostructures surrounded by self-assembled monolayers (SAMs), are used for the detection and discrimination of VOCs. Through a simple and judicious design process, involving changes in pH and water content of peptide solutions, a 5 element biohybrid sensor array coupled with a gas phase surface plasmon resonance imaging (SPRI) system, is shown to achieve sufficient discriminatory capabilities for 4 VOCs. Moreover, the limit of detection (LOD) of the multi-array system is bench-marked at < 1 ppbv and 6 ppbv for hexanoic acid and phenol (esophago-gastric biomarkers), respectively. Finally, the humidity effects are characterized, identifying the dissociation rate constant as a robust descriptor for classification; further exemplifying their efficacy as novel biomaterials in the field of artificial olfaction.

Introduction

Electronic noses (e-noses) are biomimetic devices inspired by mammalian olfaction.[1] They are composed of a cross-reactive chemical sensor array, with sensors working in tandem, to generate combinatorial profiles for the sensitive and selective detection of volatile organic compounds (VOCs). In this context, partial specificity of sensing elements is a key requirement, i.e. they respond broadly to a large range of VOCs.[2] However, this comes at a cost to the selectivity of the sensors. To counteract this, e-noses utilize multi-sensor arrays, which rely on the diversity of multiplexed responses. Its discriminatory capability is reliant on the response vector contrast, through which pattern recognition systems involving machine learning algorithms[3] are used for the identification and classification of VOCs. In this regard, the functionality of an e-nose has two major facets: one in its ability to detect trace levels of VOCs and another to discriminate between them.

To achieve this, hierarchical nanostructuration of the sensing layer has been a major strategy, extensively reported with non-biological chemoresistive materials.[4–6] Among them, metal oxide layers[7,8] and 2D nanomaterials[9] have been gaining traction, for their potential

in achieving multi-dimensional heterostructures.[10] In some cases, we see the explicit use of artificial nanostructures to elicit a function complementary to its biological counterpart, such as capillary-mimicking scrolling graphene nanosheets, which were shown to increase the sensor response.[11] More often than not, structure is merely used as a tool to enhance array sensitivity and response diversity to boost, the later facet of, discrimination.[8] However, the nanostructuration of these non-biological surfaces relies on multi-step, fabrication processes typically using either, top-down approaches (requiring multiple mechanical/chemical exfoliation such as lithography, etching, etc.) and/or bottom-up approaches (requiring chemical synthesis and processes such as chemical vapor deposition, epitaxial growth, etc.). Besides the need for expensive instrumentation, these processes are usually difficult to scale up and a multi-sensor array further complicates the production pipeline, where individual sensors need to be addressed independently.

To overcome arduous and time consuming nanostructuration processes, for the past two decades, materials science research has sought to exploit self-assembly principles ubiquitous in nature. Both biological and synthetic building blocks have been used to build artificial materials with hierarchical nanostructures, which offer customizable properties to fabricate functional devices.[12] Surprisingly, to the best of our knowledge, self-assembled, multi-structural, bioarchitecture for an e-nose application has not been studied. We believe the reason lies predominantly with structural integrity and functional stability expected of these biological heterostructures when working under dry, gaseous conditions. Recently, our group reported an e-nose utilizing peptide-based self-assembled monolayers (SAMs) as sensing elements.[13,14] The device used surface plasmon resonance imaging (SPRI) as a unique gas-phase optical transduction system,[15] with multiplexing capabilities. Its functionality was exemplified by its ability to distinguish between VOCs differing by a single methylene group[13] and even between chiral molecules.[3] The subsequent commercial valorization and product adoption[16] established the efficacy of such peptide-based sensor arrays. Thus, peptides, in the form of SAMs, have been shown to offer exceptional stability as robust sensing materials for VOC

analysis. Herein, we are interested in diversifying the structural heterogeneity of such sensing elements to obtain novel binding properties for VOCs.

Bioarchitecture with peptides was first introduced by Zhang *et al.* in the early 1990's[17] with self-assembling peptides. Thanks to their simple structure and ease of synthesis, peptides have been considered an effective family of structural sub-units for bottom-up structuration of complex nanobiomaterials. Furthermore, peptides also offer a wide range of physicochemical properties that allow them to self-assemble into various molecular configurations.[12] Within this large family, surfactant-like peptides (SLP), also commonly referred to as 'peptide detergents'[18] or 'lipid-like peptides',[19] are a class of short amphiphilic peptides[20] (typically < 10 residues) which have a hydrophilic head and a hydrophobic tail. SLPs are about $2-3\,\mathrm{nm}$ in length, consisting of a head group with $1-2$ amino acids and a tail group with several consecutive hydrophobic amino acids.[21] The head group is usually composed of a negatively charged residue for anionic amphiphiles, such as glutamic acid and aspartic acid,[22] or a positively charged residue for cationic amphiphiles, such as arginine, lysine or histidine.[23,24] SLPs have gained popularity owing to this ability, reportedly forming an assortment of ordered hierarchical structures such as: bilayers, nanotubes, nanovesicles,[25,26] nanofibers and globular aggregates.[18,27] As a result of their structural properties, SLPs have shown tremendous potential in a wide range of applications such as: antimicrobial materials,[28] vectors for drug delivery,[19] templates for biomineralization,[29] membrane protein stabilization[30] and hydrogel scaffolds in regenerative medicine.[31]

In this work, through the judicious design of a SPRI chip, for the first time we show that it is possible to use the principles of peptide self-assembly to develop structurally contrasting 'biohybrid' sensing surfaces for the sensitive detection and discrimination of VOCs. For this purpose, we introduce a designer SLP sequence: $\mathrm{CG_7{-}NH_2}$, with a cysteine (Cys) residue for the head group, 7 repetitive glycine (Gly) residues for the tail group where the $C-$terminal ($C-ter$) is amidated. Beyond its ability to self-assemble into various supramolecular nanostructures, we demonstrate the novelty of this sequence by immobilizing

these nanostructures onto Au surfaces of the SPRi chip for e-nose development. Following their functionalization, we characterize the multi-structural biohybrid surfaces with atomic force microscopy (AFM) measurements. Thus, by understanding and exploiting customizable mechanisms of the CG_7-NH_2 self-assembly, we design 5 biohybrid sensing elements and test 4 VOCs, to effectively adjudicate the structural heterogeneity and its functionality as an e-nose multi-sensor array. We observe that CG_7-NH_2 biohybrid surfaces are highly sensitive and are capable of detecting trace levels of VOCs. Moreover, despite only being made up of a single sequence, the sensing elements are morphologically and physicochemically divergent enough to effectively discriminate between them. Simultaneously, we proceed to characterise the humidity effects and divulge the water vapor adsorption mechanisms at play on these surfaces and their impact on VOC sensing. We believe this study will act as an initial proof-of-concept, offering a road map for SLP design and biohybrid surface fabrication, for their use and potential integration into functional multi-sensor arrays for e-nose applications.

Results and Discussion

Biohybrid Structuration of Sensing Elements

SLP Design and Considerations

When selecting the head group for the SLP the priority was with regard to their immobilization for chip preparation. Therefore, we opted for a single residue of Cys for thiol-mediated immobilization on the Au surface of the SPRI prism. The polarity and by extension the hydrophilic nature of the head group was achieved by assigning a net charge to the SLP monomer. This was done by placing the Cys at the $N-$terminal ($N-ter$) with no capping, while the $C-ter$ was amidated (see figure 1(a)). The ESI-MS spectrum of CG_7-NH_2 is shown in figure $S1$, Supporting Information. The unique advantage of this approach was the ability to trigger self-assembly by $pH-$stimulated charge-conversion.[32] When the envi-

ronmental $pH < 8.2 = pKa$, the $N-ter$ was protonated, making CG_7-NH_2 a functional cationic SLP. Figure 1(b) shows the electrostatic potential energy distribution for the solvent accessible surface[33,34] of CG_7-NH_2 at $pH = 4.7 < 8.2 = pKa$. The positive charge distribution of $N-ter$ can be visualised, in correspondence with the traditionally used dimethyl sulfoxide (DMSO)-based binary mixture with 65 % water - $DW65$.[13]

For the tail group, in spite of more hydrophobic side-chains being favorable for self-assembly,[35] we chose Gly with the lowest hydropathy index -0.4 (see figure 1(a)). Considering the increased hydrophilic nature of a plasma-treated Au surface.[36] This ensured effective SAM immobilization within the $18h$ self-assembly window.[13] Furthermore, to maximise the potential for contrasting morphologies, we aimed at attaining a majority of high-aspect ratio nanostructures (nanofibers). Therefore, the length of the tail group was set to 7 repetitive Gly residues.[37]

Mechanisms of Supramolecular Self-assembly in Solution

To confirm nanofiber formation in solution, 0.1 mM of CG_7-NH_2 (which was estimated to be above the Critical Aggregation Concentration (CAC)[18]) was eluted in $DW65$. Following which, $DW65-0.1$ mM SLP was sonicated for 15 mins to facilitate the nucleation of the SLP aggregates and left at 25°C for $4-5$ hours to self-assemble (see figure 1(c)). The TEM image (see figure 1(d)), primarily, revealed the presence of 3 types of structures: (i) nanofibers, (ii) globular aggregates and (iii) branched nanofibers (see figure 1(c) & (d-inset)).

For the nanofibers, a stringent diameter of 6.0 ± 0.9 nm was observed (see figure 1(e)), which was approximately $2\times$ the extended length of CG_7-NH_2 (see figure 1(b)). Thus, it can be speculated that the initial stage of self-assembly process involves the hydrophobic collapse of the tail groups, acting as thermodynamic instigators propelling SLP monomers to aggregate. In this primary nucleation step, while the hydrophobic tails pack together, the charged polar head groups are oriented towards the surface of the nanostructures facilitating hydration. The repulsive electrostatic interactions between the charged residues dictate the

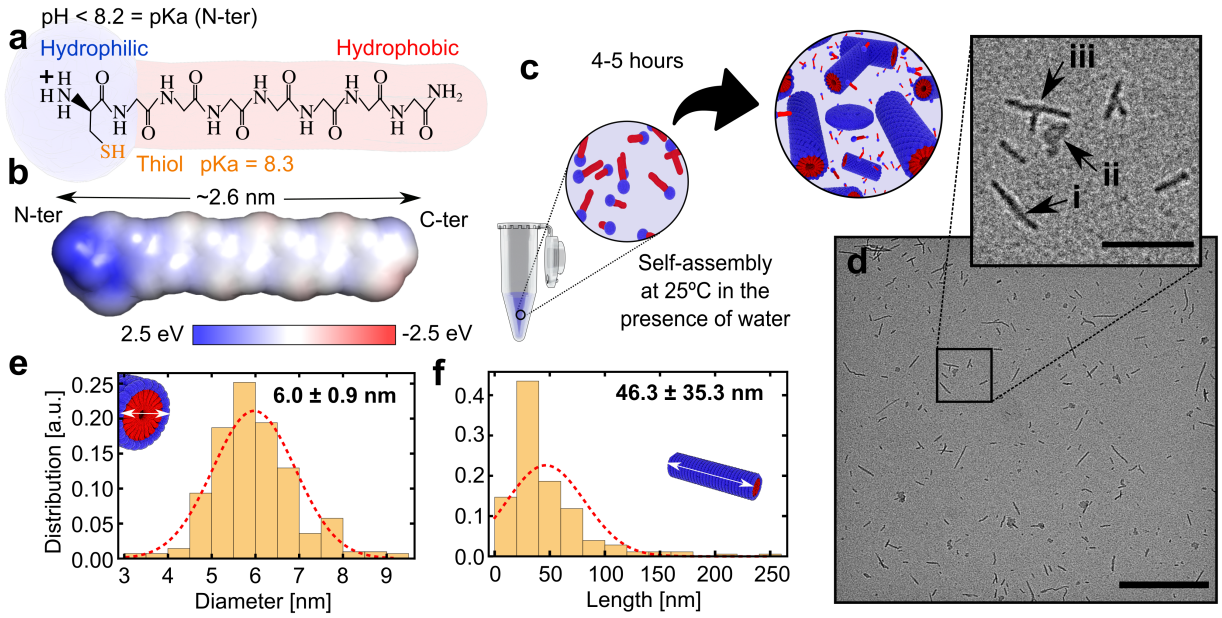

Figure 1: Supramolecular structures in solution. **(a)** The molecular structure of $CG_7{-}NH_2$, with length $\sim 2.6\,\text{nm}$, showing the protonated state of the $N-ter$ at $pH < 8.2 = pKa$. Note that there is a deprotonation of the thiol group at $pH > 8.3 = pKa$ of Cys. The hydrophilic and polar head group is represented in blue whereas the hydrophobic tail is represented in red to visually signify their self-assembling mechanism. The thiol group is accented in orange. **(b)** Electrostatic potential (kBTe (in eV)) mapped onto the solvent accessible surface of $CG_7{-}NH_2$ in the $DW65$ ($pH = 4.7$) at 25°C. Initially, the pKa values at $pH\,4.7$ were calculated using the PDB2PQR server[34] with the PARSE forcefield, which allowed the $C-ter$ to be neutralised. For the sake of experimental relevance, the dielectric constant of the solvent was set to 65 based on the binary mixture of DMSO (35 %) and water (65 %).[38] Then using the APBS plugin,[33] in PyMOL, the electrostatic potential energy distribution was solved with grid spacing $0.1\,\mathring{A}$ at 25°C, and mapped onto the solvent accessible surface of the molecule. **(c)** Schematically illustrates the time-dependent self-assembly process of $CG_7{-}NH_2$ in solution, showing all supramolecular assemblies and unassembled monomer units expected to be present in solution. **(d)** TEM image taken of $DW65 - 0.1\,\text{mM}$ SLP solution after $4-5\,\text{hours}$. Scale bar is 400 nm. **(inset)** Highlights 3 types of nanostructures suspended in solution: (i) nanofibers, (ii) globular aggregates and (iii) branched nanofibers. Scale bar is 100 nm. **(e)** Nanofiber diameter distribution: average diameter $= 6.0 \pm 0.9\,\text{nm}$ **(f)** Nanofiber length distribution (including branched nanofibers): average length $= 46.3 \pm 35.3\,\text{nm}$.

curvature of the nanostructures. Simultaneously, extensive hydrogen bonding networks stem from the SLP side-chains. These interactions have been related to the formation of $\beta-$sheet structures, which are essentially the primary structural motifs of the nanofibers. As opposed to the hydrophobic interactions, hydrogen bonds are directional and endow structural order to these motifs, which propel axial growth leading to nanofiber elongation. In this regard, the nanofiber lengths were highly poly-dispersed with an average value of 46.3 ± 35.3 nm (see figure 1(f)), pointing to the nanofibers undergoing dynamic self-assembly at different stages of progression. Simultaneously, we also noticed branched nanofibers (see figure 1(d-inset)), which point to secondary nucleation on the surface of the initial fibrillar nanostructures.[39] The globular aggregates, on the other hand, have been reported to lack $\beta-$sheet structures,[40] resulting in highly variable shapes and sizes (see figure 1(d)). It can be reasoned that these unordered structures fuse together more readily, where the repair of the structural and energetic imbalances[41] are facile. All these nanostructures together with the unaggregated monomers are, therefore, seen to be present in the solution (as schematically represented in figure 1(c)).

As a means of assessing the temporal evolution of the self-assembly process, the solution was left, at 25°C, for an additional 3 days. On inspection, the nanofibers had lengthened and interconnected to form mesh like nanostructures (see figure $S2$, Supporting Information). Therefore, as the nanofibers lengthen with temporal progression, they aligned and fused together to form longer interwoven structures. Similarly, the globular aggregates had also fused together to form larger, less dense aggregates, which surrounded the interweaving nanofibers. A study by Wang *et al.*[41] further corroborated to this mechanism and the time-dependent advancement of SLP self-assembly; accentuating the self-healing process at the connecting ends of the aligned fibres. Even though these larger multi-structural aggregates offer a variation in morphology, their tendency to precipitate negatively impacts the droplet-based inkjet microarray fabrication processes, leading to reproducibility issues. Therefore, such experimental conditions were no longer considered in this study.

Structural Characterization of Biohybrid Surface Architecture

To validate the immobilization of the nanostructures on the Au surface, 0.5 μL of the $DW65-0.1\,\mathrm{mM}$ SLP solution was spotted onto Au-coated glass slides. The slides were then placed in a humidity controlled chamber at relative humidity (RH) 94 % to mitigate droplet evaporation, which was conducive to the self-assembly process. Under humid conditions, SAMs were left to form for 18 hours. By spotting immediately after the agitation step, we were able to easily integrate this bottom-up structuration strategy into our existing chip fabrication protocol.[13] Moreover, this also ensured that after primary nucleation[39,42] the nanostructures were sufficiently dispersed in the droplets and their oligomerization did not hinder microdroplet dispensing. The temporal coordination of the two simultaneous self-assembly mechanisms, also meant that the secondary nucleation and growth[39,42] of the nanostructures occurred within the droplet, before they eventually sediment onto the Au surface. After spotting, the added weight of these nanostructures and their tendency to chemisorb onto the hydrophilic Au surface hastened their immobilization on the Au surface. Indeed, now with the abundance of *Cys* in contact with the Au surface, Au-S bonds were formed, essentially anchoring them sturdily onto the surface. Figure 2(a) & (b) show the AFM topographic and phase images of the $DW65-0.1\,\mathrm{mM}$ SLP spot after self-assembly, multiple rinsing steps and drying. Note that the term 'spot' refers to the region in which the droplet was in contact with the Au surface. The immobilization process takes place within its boundaries. Therefore, AFM scans were taken at the center of the spots. On top of the three forms of supramolecular nanostructures: (i) nanofibers, (ii) globular aggregates and (iii) branched nanofibers, we would like to introduce (iv) nanofiber stacks immobilized on the Au surface.

Besides these supramolecular assemblies, unaggregated SLP monomers are also evenly distributed within the droplets (see figure 1(c)). After spotting, they most likely initiate the second self-assembly phase, forming SAMs around these nanostructures. Even though SAMs were not easily distinguishable on the AFM scans, their presence can be discerned

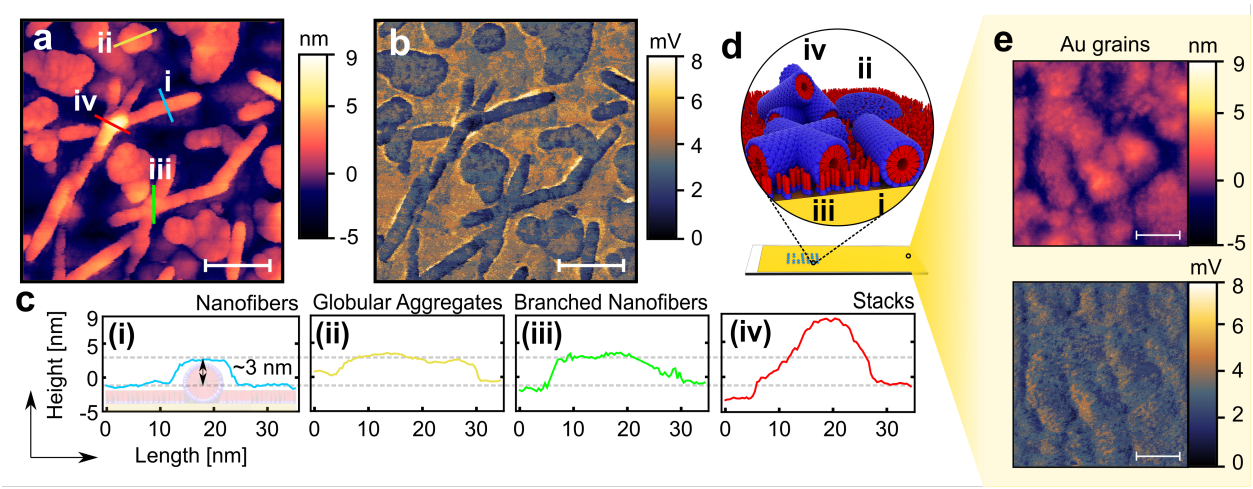

Figure 2: Hierarchical nanostructures immobilized on the Au surface. **(a)** AFM topographic image and **(b)** AFM phase image of an $0.5\,\mu$L $DW65-0.1\,$mM SLP spot on an Au-coated glass substrate. The scan was made at the center of the spot after $18h$ of immobilization followed by rinsing and drying of the substrate. Scale bars are 50 nm. **(c)** Height profile of representative **(i)** nanofibers, **(ii)** globular aggregates, **(iii)** branched nanofibers and **(iv)** nanofiber stacks. A schematic cross-section of a nanofiber surrounded by SAMs is superimposed on the nanofiber profile. **(d)** Schematically illustrates the 'biohybrid' surface highlighting its 4 possible constituents. **(e)** AFM **(Top)** topographic image and **(Bottom)** phase image of Au grains on bare Au surface. Scale bars are 50 nm.

via the height profiles of the nanofibers cross-section (see figure 2(c-i)), globular aggregates (see figure 2(c-ii)) and branched nanofibers (see figure 2(c-iii)). A height of only $\sim 3\,$nm, equivalent to a single monomer unit, was seen for these nanostructures, suggesting the presence of SAMs surrounding the relative denser hierarchical assemblies (see figure 2(d) and figure $S3$(a) & (d), Supporting Information). A further dichotomy between the hierarchical nanostructures and SAMs was apparent on the phase image (see figure 2(b)), where the differences in softness and adhesion were exhibited as changes in color contrast.[43] The first indication of SAMs was the absence of the grain boundaries in the phase image (see figure 2(b)) as opposed to a bare Au surface (see figure 2(e-Bottom)). Moreover, SAMs seemed to increase the softness of the surface with a comparably higher phase change. This aspect was further validated with a phase image at the boundary of the spot (see figure $S3$(c), Supporting Information).

The high aspect ratio globular aggregates added multiplicity to the sensing elements.

Their lack of structural order allowed them to spread bidirectionally over a larger area on the Au surface. In the case of branched nanofibers, we hypothesize that besides secondary nucleation, two stacked strands also may have the tendency to self-heal both in solution and after deposition (see figure 2(a) & (c-iii)). However, the self-healing process does not always occur, considering the densely packed, ordered nature of these nanofibers, which preferentially fuse along their axial ends. This brings us to the stacked nanostructures (see figure 2(a) & (c-iv)), where part of the structures were immobilized on the Au surface while the rest were stacked on top of each other. Even visible on the TEM images (see figure 1(d)), we believe they are a result of overcrowding. Primarily composed of nanofibers, these stacks formed rigid and dense clusters based on the number of nanofibers and their fully/partially fused nature. Henceforth, due to the large structural heterogeneity of these surfaces, they will be collectively referred to as 'biohybrid' surfaces. Figure 2(d) schematically illustrates the different structural constituents of a $CG_7{-}NH_2$ biohybrid surface.

Tuning Biohybrid Surface Architecture of Sensing Elements

Herein, we intended to diversify such biohybrid surfaces and use them as sensing elements for the development of a novel biohybrid multi-sensor array. An important aspect of tuning surface morphologies lies in the mechanistic aspect of an dynamic equilibrium between the monomer and the resulting self-assembled nanostructures, in solution (schematically represented in figure 3(a-i)). Thus, by changing the condition of the spotting solution we were able to favor one or more of the different types of structural entities present in solution, which in turn influenced the nature of the resulting biohybrid surface. 2 parameters of the traditional $DW65$ solution were varied: the water content ($DMSO$ and $DW35$) and pH ($DW65H$ and $DW65L$). The target properties of the 5 different solutions are listed in figure 3(a-ii). Besides the 0.1 mM, two other SLP concentrations were tested for all these solutions: at 0.01 mM and 0.5 mM. Moreover, different chips including; Au-coated glass slides and Au-coated prisms were spotted with these 15 solutions, simultaneously. Au-coated glass

slides were used for AFM characterisation, because they were flatter and didn't require a holder for support, enabling robust, repeatable, AFM scans. To ensure valid comparability between the two types of chips, the average Au-grain geometries were evaluated and compared for both of them (see figure $S4$, Supporting Information). Even though the average vertical dimension of a grain a_z was $\sim 2\times$ smaller than that of the SPRI prism, the lateral dimension $a_{x,y}$ and grain counts were almost comparable for the Au-coated glass slide. Due to $a_{x,y} \gg a_z$, the flexible hierarchical nanostructures were expected to behave similarly on both samples, following the topography of Au surface during their sedimentation process (as seen in figure 2).

Based on the previously discussed characteristics of the structural composition of the biohybrid surfaces, AFM scans of the flat Au-coated glass slides (see figure 3(b)-(f) and figure $S5$(a)-(e), Supporting Information) were used to quantitatively identify the different clusters of nanostructures and their relative abundance on the biohybrid surfaces. The 3σ value (99.7 % of the distribution), of the first Gaussian (black line), for all images (see figures 3(b-i)-(f-i)) was averaged $h_1 = 3.0 \pm 0.2\,\text{nm}$, which was comparable to that of average grain height of a bare Au surface (see figure $S4$(c), Supporting Information). It indicated that the SAMs, our first structural group, spanned over the entire spot surface, perfectly following the topography of the grains. The individual nanofibers, branched nanofibers and globular aggregates, were the second structural group. The second Gaussian (blue line) had an average $h_2 = 4.4 \pm 0.5\,\text{nm}$, which, as expected, was approximately $2\times$ the monomer unit. The third Gaussian (red line) was more of a quantitative measure of the relative amount (average weight of the Gaussian) for the stacked structural group, with a mean values $\mu > 3\,\text{nm}$.

Moreover, in preparation for the e-nose application, we concomitantly characterised the microarray on the Au-coated prisms using SPRI. In this way, we were able to have a complementary view of the nanoscopic and microscopic nature of the biohybrid sensing elements. Accordingly, using the two techniques, we will be analysing the effects of concentration, water and pH, which were the primary parameters varied for structural tuning.

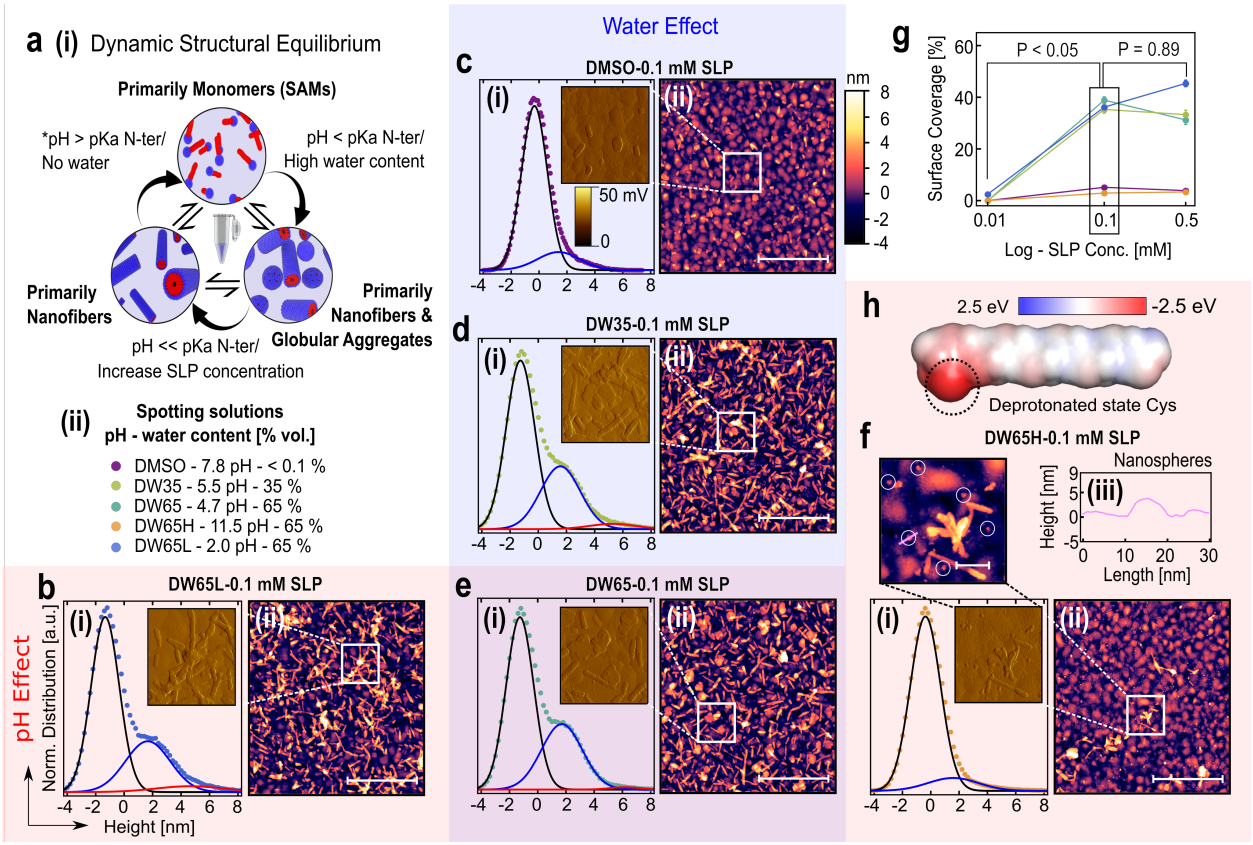

Figure 3: Tuning biohybrid nanostructuration on the Au surface. **(a) (i)** Schematic illusion of the dynamic structural equilibrium in solution. * Note that even though monomer units were favored, $pH > 8.2 = pKa$ of the $N-ter$ led to the deprotonation of Cys with $pKa = 8.3$. **(ii)** The measured pH of the 5 spotting solutions and water content (in % vol.): **(b)** $DW65L-0.1\,\text{mM}$ SLP, **(c)** $DMSO-0.1\,\text{mM}$ SLP, **(d)** $DW35-0.1\,\text{mM}$ SLP, **(e)** $DW65-0.1\,\text{mM}$ SLP and **(f)** $DW65H-0.1\,\text{mM}$ SLP **(i)** Normalized height distributions of $1\times1\,\mu\text{m}^2$ and $2\times2\,\mu\text{m}^2$ (see figure $S5$, Supporting Information) fitted with a Gaussian mixture model (see Supporting Information for details). Note that the mean height value was set to zero. **(ii)** $1\times1\,\mu\text{m}^2$ AFM topography images. The scans were made at the center of each spot. All scale bars are 400 nm. **(inset)** Enlarged peak-force error images give a qualitative topometric view to reveal fine surface details.[44] **(f-iii)** Height profile of a representative nanosphere on the $DW65H-0.1\,\text{mM}$ SLP spot. Enlarged topography image with circled nanospheres. Scale bar is 50 nm **(g)** Line chart showing the hierarchical nanostructured surface coverage for the 5 conditions at the 3 SLP concentrations. The values (in %) for all 15 conditions were evaluated using $1\times1\,\mu\text{m}^2$ topographic images using Gwyddion, by manually masking the hierarchical nanostructures with a height threshold. Error bars show 0.2 nm deviation from the threshold. See the additional non zero AFM topography images in figure $S6$(a)-(e) & (f-ii), Supporting Information. A variance test was performed between each concentration group, of which, the p-values have been listed on the plot. **(h)** Electrostatic potential (kBTe (in eV)) mapped onto the solvent accessible surface of $CG_7{-}NH_2$ in the $DW65H$ ($pH = 11.5$) at 25°C. The deprotonated state of Cys is circled. Procedure discussed in figure 1(b) was followed.

SLP Concentration Effects

In relation to the work of Qui *et al.*,[18] so far, we have considered a SLP concentration of 0.1 mM to be close to the CAC of $CG_7{-}NH_2$. In order to validate the impact of concentration on the density of the immobilized hierarchical nanostructures, surface coverage values were calculated from $1 \times 1\,\mu m^2$ AFM scans for the 15 conditions. As expected, the 0.01 mM SLP concentration, being well below the CAC, showed no hierarchical nanostructuration for most solutions. The exception was $DW65L - 0.01$ mM SLP, the condition that most favored hierarchical self-assembly ($pH = 2 \ll 8.2 = pKa$). Its spots had a couple of aggregated nanofibers and globular aggregates sparsely scattered on the surface (see figure $S6$(c), Supporting Information). For all 0.5 mM SLP solutions, even with a 5-fold increase in concentration, the surface converges were almost comparable to that of the 0.1 mM SLP solutions $P = 0.89$ (see figure 3(g)). There was a saturation in the amount of nanofibers and globular aggregates immobilized on the surface ($< 50\,\%$ coverage). It can be surmised that due to overcrowding the loosely immobilized nanostructures were probably washed away during the rinsing process. Therefore, even though higher SLP concentrations generated larger quantities of supramolecular assemblies, in solution, there was a space limitation on the Au surface for effective immobilization.

We have also characterized all the spots of the 15 conditions on the Au-coated prisms using SPRI (see figure 4(a) & (b)). In spite of the surface coverage saturation noticed on the AFM images, substantial SPRI angular response curve shifts for the 0.5 mM SLP spots pointed to an increase in the mass adsorbed (see figure 4(c)). By analysing the SPRI Transverse Magnetic (TM) image at a fixed working angle $\theta_w = 42.5°$, we were able to visualize these larger intensity variations between the spots of the two concentration groups (see figure 4(b)). Since there was surface coverage saturation, it was assumed that the mass increase was primarily a result of denser SAMs. Through the phase images of $DW65L - 0.1$ mM SLP (see figure $S6$(g-i), Supporting Information) and $DW65L - 0.5$ mM SLP (see figure $S6$(f-i), Supporting Information), we were able to qualitatively gauge the density of SAMs surround-

ing the hierarchical nanostructures. Darker contrast, free of grain boundaries, was a clear indication of denser SAMs for $DW65L - 0.5\,\text{mM}$ SLP compared to $DW65L - 0.1\,\text{mM}$ SLP. For SPRI sensing purposes, array sensitivity was also an important consideration. In this regard, for the 0.5 mM SLP concentration group, there was also a flattening of the angular response curves, which resulted in significant angular sensitivity $\partial R/\partial\theta$ losses (see figure 4(c-inset)). Intuitively, we can assume that as the surface got denser so did its potential for surface plasmon polarization (SPP) damping. Therefore, ideally, the concentration needed to be above the CAC, to achieve biohybrid nanostructuration, yet low enough to ensure that the sensitivity losses weren't substantial. Moreover, since we were utilising an intensity modulated system, it was imperative that θ_w was fixed. By having less divergent angular response curves, we were able to pick θ_w within the dynamic ranges of the entire sensor array. The 0.1 mM SLP concentration group best fits these biohybrid sensing surface requirements for $CG_7{-}NH_2$. A bulk refractive index sensitivity $\partial R/\partial n$ range of $5800 - 6800\,\%/\text{RIU}$ was evaluated for this group. It was within the sensitivity range of $6600\,\%/\text{RIU}$ with comparable ranges for all 5 spots (see figure $S7$, Supporting Information).

Another consequence of higher SLP concentration seemed to be an increase in nanofiber diameter (see figure $S6$(f-ii,iii) & (g-ii,iii), Supporting Information), where an average diameter of $7.2 \pm 1.5\,\text{nm}$ for $DW65L - 0.1\,\text{mM}$ SLP was seen to rise to $11 \pm 1.6\,\text{nm}$ for $DW65L - 0.5\,\text{mM}$ SLP. For one, the nanofibers obtained at $DW65L - 0.1\,\text{mM}$ SLP showed larger diameters than the ones initially estimated using the TEM ($6.0 \pm 0.9\,\text{nm}$). This was attributed to the AFM tip convolution effect. Furthermore, to rule out tip-induced nanofiber deformation, phase images (see figure $S6$(f-i) & (g-i), Supporting Information) were used to qualitatively emphasize similar stiffness characteristics. Meaning that nanofibers in both samples would induce this effect, if any. Therefore, it was likely that at higher SLP concentrations the initial, primary, structural motifs were larger in diameters. As a result, we like to address the contentious characteristic of the presence of a inner cavity in a self-assembled SLP nanofiber. As proposed by Colherinhas *et al.*[45] in a molecular dynamic study, it was

likely that these nanofibers were in fact tube-like with sub-nanometric cavities.

Water Content Effects

Figure 3(c), (d) & (e) show the biohybrid surfaces for spotting solutions $DMSO - 0.1\,\mathrm{mM}$ SLP, $DW35 - 0.1\,\mathrm{mM}$ SLP and $DW65 - 0.1\,\mathrm{mM}$ SLP, respectively, listed in the order of increasing water content. $DMSO - 0.1\,\mathrm{mM}$ SLP spotting solution, which only contained $DMSO$, had a $pH = 7.8$ slightly below the $8.2 = pKa$ of the $N-ter$. The resulting biohybrid surface had a small quantity of nanofibers and globular aggregates (see figure 3(c-i)). DMSO was considered a denaturant; highly destructive towards non-covalent species that were based on a combination of hydrophobic interactions and hydrogen bonding.[46] Even though the $DMSO - 0.1\,\mathrm{mM}$ SLP solution was only supposed to contain very low quantities of water (purity $\geq 99.9\,\%$), by placing the samples droplets in high humidity conditions ($94\,\%\,\mathrm{RH}$), we inherently increased the trace levels of water ($< 0.1\,\%$ vol.) within these droplets. A study by Wang *et al.*,[47] reported the decisive role played by trace quantities of water, brought about by humidity changes, in triggering self-assembly of a biologically derived dipeptide. Here we would like to expand its scope to SLPs, emphasizing the necessity in considering environment humidity changes when fabricating biohybrid structures as functional materials.

Increasing the water content by $35\,\%$ vol., with $DW35$, resulted in longer nanofibers densely populating the Au surface, with a notable presence of nanofiber stacks characterised by the third Gaussian of the height distribution (see figure 3(d-i)). Nevertheless, upon further increase to $65\,\%$ vol., with $DW65$, we saw a structural transition favoring the formation of globular aggregates (see figure 3(e-ii)). Owing to their high aspect ratio, $DW65{-}0.1\,\mathrm{mM}$ SLP had the highest surface coverage for the 0.1 mM SLP concentration group (see figure 3(g)). Supporting the work of Deshmukh *et al.*,[48] it can be reasoned that the nanofiber to globular aggregate transition was due to the strong solvation effect of the *Gly*-based hydrophobic tail.[49] More water promotes the formation of solvation shells[50] around the hydrophobic tail, which, by preventing $\beta-$sheet formation favor unordered aggregates. This hypothesis was

supported by the lack of globular aggregates on the $DW65-0.5\,\mathrm{mM}$ SLP biohybrid surface (see figure $S6$(d), Supporting Information), leading to a substantial decrease in its surface coverage compared to $DW65-0.1\,\mathrm{mM}$ SLP (see figure 3(g)). Therefore, by increasing the monomer concentration in $DW65-0.5\,\mathrm{mM}$ SLP, we are likely reducing the relative water molecules constituting the solvation shells, which, in turn, favors nanofiber assemblies.

Interestingly, a ring-effect, usually associated with the evaporation of sessile droplets, was observable with the SPRI-TM image of the high concentration spots: $DMSO-0.5\,\mathrm{mM}$ SLP, $DW35-0.5\,\mathrm{mM}$ SLP and $DW65-0.5\,\mathrm{mM}$ SLP (see figure 4(b)). Opposite to what is usually observed, the denser spot interior compared to the outer ring was associated with the temporal progression of the self-assembly process. Considering the hierarchical nanostructure saturation, this was more related to the second self-assembly process of the SAM taking place within the contact lines of the receding droplets. Moreover, with the low water content solutions ($DMSO$ and $DW35$) we noticed a mixed droplet evaporation behaviour,[51] where the contact line of the droplet was pinned at one point via constant contact radius (CCR) evaporation mode while the other parts unpinned and receded via constant contact angle (CCA) mode[52] (see figure 4(b)). By increasing the water content, with $DW65$, we saw a transition to a complete CCA evaporation mode, where contact line was seen to recede more evenly (see figure 4(b)). Furthermore, $DW65$ and $DW35$ spots, which were populated with hierarchical nanostructures, showed the coffee ring-effect, where we saw an accumulation of mass on the contact line.[53] The capillary flow of liquid towards the contact line of the droplets led to larger structural agglomerates at the previously pinned ends (as accented by the red arrows on figure 4(b-ii,iii & v)). Even though, microscopically, it wasn't as distinct on the $0.1\,\mathrm{mM}$ SLP concentration group, nanoscopically, the coffee ring-effect was discernible. In fact, these larger agglomerates of the hierarchical nanostructures were recognizable (see figure $S3$, Supporting Information). $DMSO-0.1\,\mathrm{mM}$ SLP and $DMSO-0.5\,\mathrm{mM}$ SLP spots also resulted in much larger agglomerates, which were scattered throughout the entire spot area (see figure 4(b)). The rather noisy line profile of the $DMSO-0.5\,\mathrm{mM}$ SLP spot, highlight

the micrometric sizes of these larger agglomerates (see figure 4(b-i)). This resulted in these sensors having the largest SPP damping effects, which was measurable by the flattening of the angular response curve (see figure 4(c)) and by extension had the highest loss in angular sensitivity (see figure 4(c-inset)).

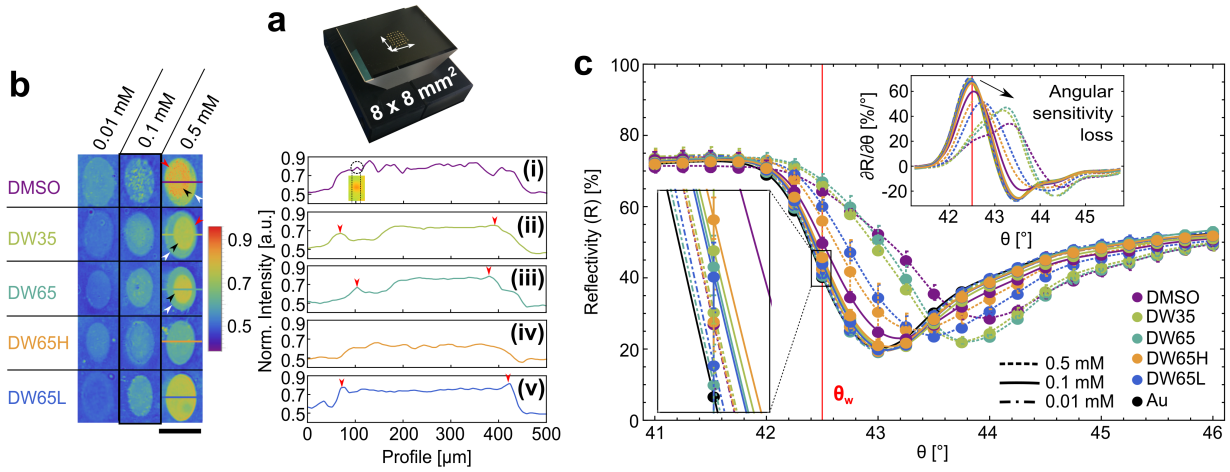

Figure 4: Characterizing the SPRI multi-sensor array. **(a)** A custom SPRI prism spotted with 5 nL microdroplets on a $8 \times 8\,\mathrm{mm}^2$ region-of-interest (ROI). **(b)** SPRI TM images of a representative spot replicate at $\theta_w = 42.5°$, listed for all 15 conditions. The intensities were normalized and the grey scale images were recolored using a color map to emphasize microscopic agglomerates. Note that the sensing elements/sensors were defined as $\sim 350\,\mu$m diameter circles at the center of the spots. Scale bar is $500\,\mu$m. The red arrows on $DMSO - 0.5\,$mM SLP and $DW35 - 0.5\,$mM SLP show a pinned contact line region where the sessile droplet evaporates with a constant contact radius (CCR) . The white arrow shows the outer spot and black arrow the inner spot, which highlights the unpinned region on the contact line that recedes maintaining a constant contact angle (CCA). **(i-v)** Line profiles of the 0.5 mM SLP concentration group. The red arrows point to coffee ring-effect. **(inset)** An example of a micrometric agglomerate. **(c)** SPRI angular response curves for the 15 spots ($\theta_w = 42.5°$ was set to maximise $\partial R/\partial\theta$ for the 0.1 mM SLP concentration group). **(inset)** Corresponding angular sensitivity $\partial R/\partial\theta$ curves.

pH Effects

The $DW65$ solution containing the highest quantity of water was adjusted by using HCl and NaOH to attain pH values far below ($DW65L$-$pH = 2$) and above ($DW65H$-$pH = 11.5$) the $pKa = 8.2$ of the $N-ter$ of CG_7-NH_2, respectively. For $DW65L - 0.1\,$mM SLP, despite the fact that the water content was high, the lower pH favored nanofiber formation resulting

in the absence of globular aggregates (see figure 3(b-ii)). The abundance of nanofibers and the resulting nanofiber stacks, in the $DW65L - 0.1\,\text{mM}$ SLP solution, was reflected by the highest amplitude of the third Gaussian (see figure 3(b-i)) compared to all other conditions in 0.1 mM SLP concentration group. As also seen with $DW35 - 0.1\,\text{mM}$ SLP (see figure 3(d)), it is likely that the nanofiber stacks were a result of higher quantities of nanofibers within the droplet, which leads to surface crowding during the sedimentation process. In this regard, $DW65L$ solution was more prone to favor nanofiber formation. Even though the surface coverage of $DW65L - 0.1\,\text{mM}$ SLP was comparably lower, a clear increase in $DW65L - 0.5\,\text{mM}$ SLP resulted in the highest surface coverage of $\sim 45\,\%$ (see figure 3(g)). A natural result of the shift in equilibrium was the compositional trade-off between SAMs and hierarchical nanostructures. Therefore, despite having the most hierarchical nanostructures, a relatively small angular response curve shift was observable (see figure 4(c)), indicating less dense SAMs. When looking at the $DW65L - 0.5\,\text{mM}$ SLP, SPRI TM-image, there was no noticeable signs of receding contact line and ring-effects. Moreover, even though a slight coffee ring-effect was still discernible, this spotting solution resulted in the most even immobilization across the entire surface of the spot.

The basic pH spotting solution $DW65H$ resulted in very limited nanostructuration (see figure 3(f)). However, amorphous aggregates were still noticeable on the surface, with an additional amount of smaller nanospheres scattered throughout the Au surface (see figure 3(f-iii)). A study by Cote *et al.*[54] elucidated the mechanism involved in these high pH conditions, pointing to dispersed monomers aggregating into amorphous spherical micelles. In analysing the electrostatic potential energy distribution for the solvent accessible surface[33,34] of $CG_7{-}NH_2$ at $pH = 11.5$ (see figure 3(h)), we noticed that the cationic SLP had transformed into an anionic SLP, instead. With a $pKa = 8.3$[55] calculated for the thiol of Cys, under extreme basic conditions, sulfur atoms were increasingly deprotonated. Therefore, as previously discussed, there was a tendency for amorphous aggregations, which, microscopically, resulted in the formation of larger structural agglomerates (see figure 4(b-iv)). These

agglomerates resulted in visible precipitates, which led to issues with microdroplet dispensation. Therefore, $DW65H$ was considered highly unstable, which was reflected in the large variation in the $DW65H - 0.5\,\text{mM}$ SLP spot replicates as shown by the error bar in the angular response curves (see figure 4(c)).

Biohybrid Sensing Elements for VOC Detection and Discrimination

The 5 spotting solutions containing $CG_7{-}NH_2$ led to different biohybrid surface architectures which were in essence ratios of the various self-assembled nanostructures. For the structural relevance, even immobilization and high angular and refractive index sensitivity, 0.1 mM SLP spots were selected to create a 5 element sensor array. The question remained to be: was the structural and physicochemical diversity of these sensing elements sufficient for the sensitive and selective detection of VOCs? To answer this, 4 different VOCs: Phenol, Butyric acid, 1-Hexanol and Hexanoic acid were tested at 25°C in the parts-per-billion ppbv/ parts-per-million ppmv ranges (see figure 5(a)-(d)).

VOC Detection

To evaluate the sensitivity, trace levels of hexanoic acid and phenol were tested in relation to a clinical study by Kumar *et al.*[56] who highlighted their significance, as volatile biomarkers, for esophago-gastric cancer detection. They reported a median concentration of 19 ppbv and 17 ppbv for the cancer cohort compared to a 10 ppbv and 6 ppbv for the healthy control group, for hexanoic acid and phenol, respectively. In order to asses and compare the limit of detection (LOD) of our structural sensor array, a concentration-dependent descriptor, known as the steady-state response $\Delta RIU(n-1)_{eq}$ (see Supporting Information for details) was extracted from the SPRI temporal response curves (see figure 5). Considering the detectable signal as 3× the noise of the system (0.05 % reflectivity shift[15]) we were able to extrapolate a LOD of < 1 ppbv and 6 ppbv for hexanoic acid and phenol, respectively (see table $S1$, Supporting Information), which were within the ranges of the esophago-gastric

cancer detection study.[56] Even though, for phenol, those low concentrations were pushing the sensing element limits, for hexanoic acid we were far above the detectable range and were limited by the concentrations detectable by our $10.6eV$ photoionization detector (PID). In relation to previously published work,[14] we believe that by increasing the wavelength of the SPRI system, even lower LODs could be potentially reached. Even so, it is important to point out that compared to the direct analysis of exhaled breath, our VOC detection was performed under ideal experimental conditions using clean, dry air as a carrier gas. Therefore, we would like to emphasize that this was merely an attempt at bench-marking the detection capabilities of $CG_7{-}NH_2$ biohybrid surfaces, with potential future adoption for trace level VOC detection in a complex milieu.

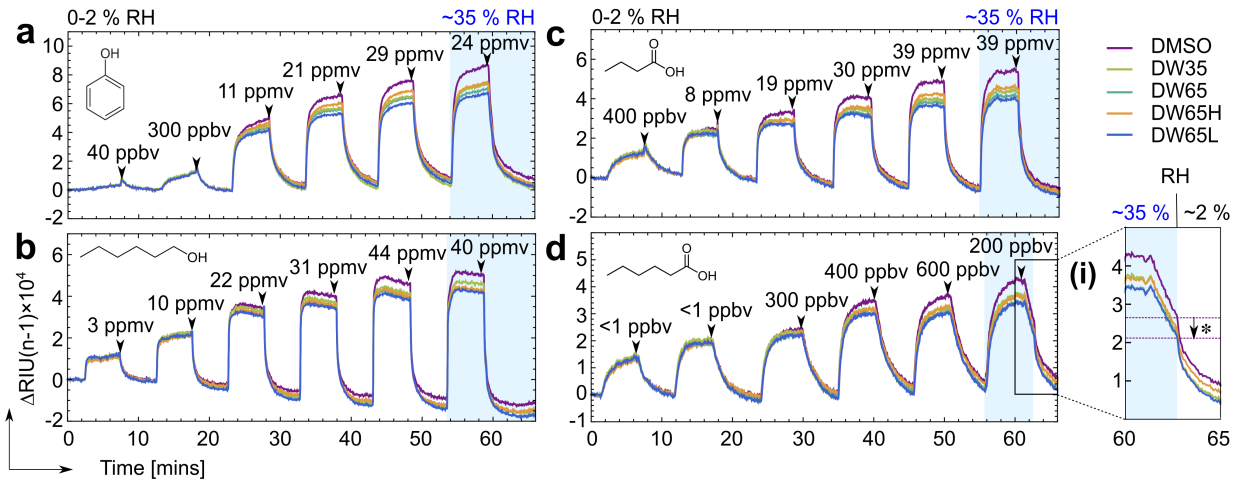

Figure 5: SPRI response as a change in refractive index $\Delta RIU(n-1)$ with time. The sensor array constituted of the 5 types of sensing elements from the 0.1 mM SLP concentration group (averaged over 3 replicates). The temporal response shows a concentration ramp of 6 VOC dose injections for **(a)** Phenol, **(b)** 1-Hexanol, **(c)** Butyric Acid and **(d)** Hexanoic Acid, performed at 25°C . The steady-state concentration of the 30 s stationary phase are listed for each dose (see figure $S8$, Supporting Information). First 5 doses were performed with a dry DHS $0-2\,\%$ RH. The 6^{th} dose was performed with humidified DHS $\sim 35\,\%$ RH. **(i)** Enlarges the instantaneous change in humidity from $\sim 35 \rightarrow 2\,\%$ RH, in the middle of the dissociation phase. * The vertical SPRI response drop for $DMSO-0.1$ mM SLP (similar to all other sensing elements) was $\Delta RIU(n-1) \sim 5 \times 10^{-5}$.

For further analysis, the steady state responses were plotted in relation to the dynamic headspace (DHS) concentrations and fitted with a empirical Freundlich adsorption isotherm

(see Supporting Information for further details). Phenol and 1-hexanol seemed to provide the stronger fit compared to the carboxylic acids, for the 5 sensors (see figure 6(a)). Regardless, a correlation of $R^2 \geq 0.98$ was observable for all fits. The convex isotherms showed favorable adsorption processes ($n > 1$) for the concentration ranges tested (see table $S1$, Supporting Information). As a matter of fact, by evaluating the Freundlich exponent 'n', we were able to notice that the $CG_7{-}NH_2$ biohybrid surfaces conveniently favored the adsorption of hexanoic acid ($n > 10$). Following which, we had phenol, butyric acid and 1-hexanol ($1 < n < 3$), with decreasing favorability (see table $S1$, Supporting Information). It can be argued that the $CG_7{-}NH_2$ biohybrid surfaces favor acidic VOCs, considering that the electron-withdrawing character of the phenyl group makes phenol more acidic than typical alcohols.

In unraveling the mechanisms involved with biohybrid/VOC interactions, $DMSO - 0.1\,\mathrm{mM}$ SLP, the sensing element hypothesized to possess the most monomer dense SAMs resulted in the largest response for all VOCs (see figure 5). We believe that the nature of SAMs allow for VOC to penetrate into the monolayer, where there is access to multiple binding sites on the Gly tail, compared to the dense hierarchical nanostructures, where the access is limited to the outer surface. Furthermore, through n we were able to gauge the energetic heterogeneity of the different sensing surfaces.[57] Table $S1$ (Supporting Information) summarises the fitting parameters: K_F the adsorption intensity and n, obtained for all the fits, arranged in the order of the conjectured increase in hierarchical nanostructuration and decrease in the SAMs monomer density. As to be expected, in general, morphological diverse surfaces with more hierarchical nanostructures seemed to increase the energetic heterogeneity of the surface. Since the polar $N - ter$ was prevalent on the surfaces, with increased nanostructuration, it can be speculated that the hydrophilic nature of the outer surfaces of these nanostructures favor the adsorption process of the polar VOCs tested.

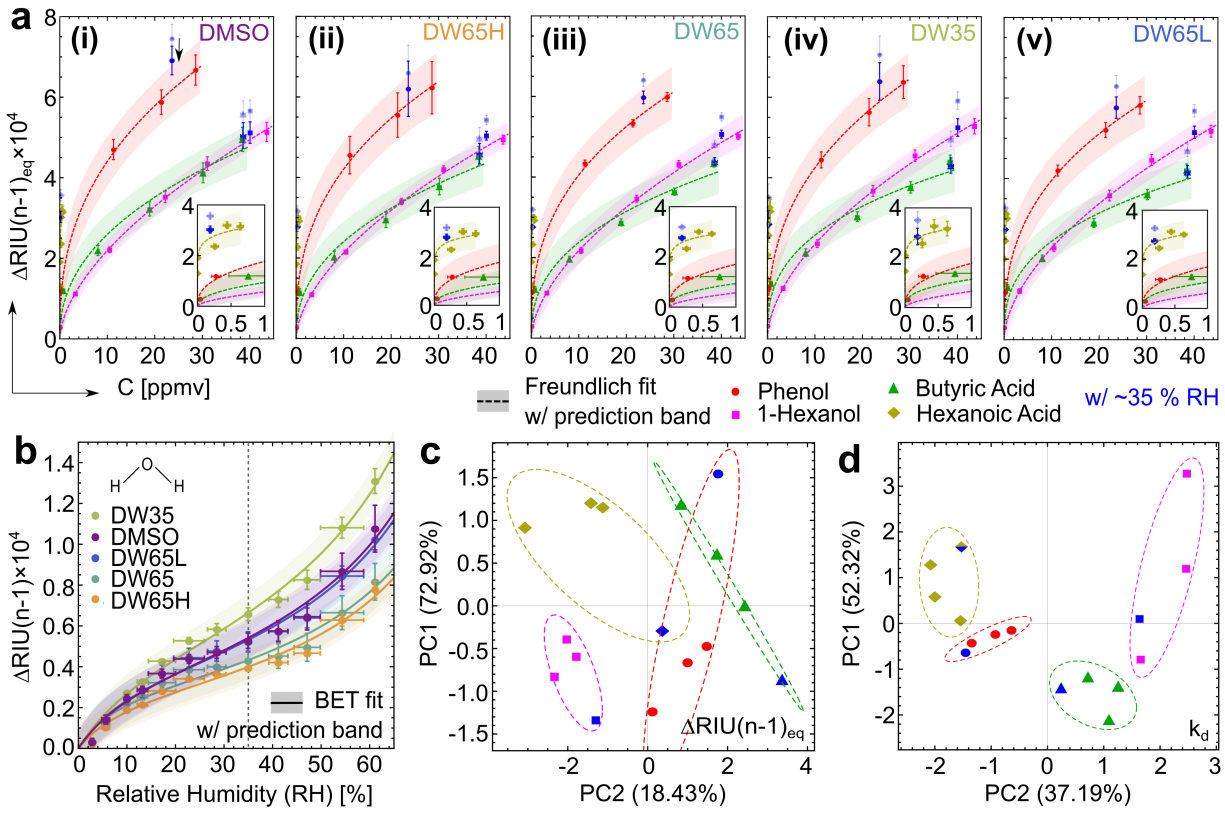

Figure 6: Elucidating Detection and Discrimination. **(a)** VOC adsorption isotherms, at 25°C, were plotted using the steady state response $\Delta RIU(n-1)_{eq}$ in relation to the measured average DHS VOC concentration . All 6 dose injections were plotted for each VOC, including the humidity corrected dose: **(i)** $DMSO - 0.1\,\text{mM}$ SLP (arrow illustrates humidity correction), **(ii)** $DW65H - 0.1\,\text{mM}$ SLP, **(iii)** $DW65 - 0.1\,\text{mM}$ SLP, **(iv)** $DW35 - 0.1\,\text{mM}$ SLP and **(v)** $DW65L - 0.1\,\text{mM}$ SLP. **(insets)** Trace VOC dose injections $(0 - 1\,\text{ppmv})$ are enlarged. All VOC/sensor adsorption isotherms were fitted with the Freundlich fit (see Supporting Information for details). For phenol and 1-hexanol with $R^2 > 0.99$, a 95 % prediction band was drawn. For hexanoic acid and butyric acid with $(0.99 > R^2 > 0.98)$ a 75 % prediction band was drawn (see table $S1$, Supporting Information for fitting parameters). Extrapolated LOD values are 6 ppbv, 230 ppbv, 50 ppbv and < 1 ppbv for phenol, 1-hexanol, butyric acid and hexanoic acid, respectively. **(b)** Water vapor adsorption isotherms (type II), at 25°C, were plotted using a dynamic relative humidity ramp and corresponding $\Delta RIU(n-1)$. All isotherms were fitted with the BET model (see Supporting Information for details) and resulted in $R^2 > 0.99$ (see table $S2$, Supporting Information for fitting parameters). A 95 % prediction band was drawn for each curve. The line at 35 % RH intersects with the points used in the humidity correction for each spot. **(c)** PCA for $\Delta RIU(n-1)_{eq}$. The two PCs accounted for 91.35 % of the total variance of the data set. **(d)** PCA for dissociation rate constant k_d. The two PCs accounted for 89.51 % of the total variance of the data set. Only the four highest dose injections were considered $\Delta RIU(n-1)_{eq} > 2 \times 10^{-4}$. The humidity corrected dose is represented in blue.

Humidity Effects

The robust nature of a sensor array, relies in its ability to offer consistent and reproducible responses. In this regard, humidity is a challenge that many e-noses and gas sensors face. As previously discussed, for application such as breath analysis, it can be a property of the carrier gas itself.[58] Therefore, humidity variations are thought to have a confounding effect on the signal, wherein, decoupling the unwanted water-related response becomes an imperative but complicated task. Hence, to initially understand water vapour adsorption on the biohybrid sensor array, the sensor responses were monitored for humidity changes between $3-62\,\%$ RH at 25°C (see figure 6(b)). Interestingly, the adsorption process resembled a type II isotherm and was similarly shaped for all the spots. As a matter of fact, this type of isotherm, fitted with its corresponding BET model (see Supporting Information for details), which was the most widely used method for predicting moisture adsorption on biologically active material[59] and structured surfaces.[60] The model describes an initial monolayer adsorption followed by a co-operative multi-layer adsorption process. The fits were used to approximate two concentration-independent parameters in this process:[61] V_m, the monolayer capacity, used for specific surface area calculations,[62] and K_B the BET constant related to the adsorption intensity (see table $S2$, Supporting Information). Here, the parameter of concern was V_m, which following its usage, increased with an increase in hierarchically nanostructured surface coverage (obtained for 0.1 mM SLP concentration group, see figure 3(g)). $DW65-0.1\,\mathrm{mM}$ SLP with the highest surface coverage, due to the globular aggregates (see figure 3(e)), gave the highest V_m. On the other hand, $DW65H-0.1\,\mathrm{mM}$ SLP, with the lowest V_m was predominantly composed of SAMs and the accessible hydrophobic tail group. We see a congruence of both the specific area and hydrophilic/hydrophobic character of the biohybrid surface, influencing the water vapor adsorption process.

Now, to divulge its influence on VOC adsorption, the 6^{th} dose injection performed with $\sim 35\,\%$ RH was analysed (see figure 5). In all cases, the humidity was seen to be an additive process which showed to positively deviate from the 95 % prediction band for phenol and

1-hexanol and 75 % prediction band for the acids. Interestingly, when corrected with the amount of water vapor adsorbed at the humidity level (see figure 6(b)) not only were we able to move within the prediction bands but in some cases (butyric acid and 1-hexanol) we saw a strong overlap with the fitted isotherms in low humidity condition. In most instances, water vapor adsorption on these biohybrid surfaces, during VOC analysis, can be seen as a purely additive process. This was further exemplified when the humidity was cut off, half way through the desorption phase of the hexanoic acid humidity infused dose injection (see figure 5(d-i)). The humidity drop seemed to occur almost instantaneously and the signal drop matched with the signal observed at 35 % RH due to water vapor adsorption, $\Delta RIU(n-1) \sim 5 \times 10^{-5}$ (see figure 6(b)). Thus, we propose an initial humidity calibration for the purposes of humidity correction. Meanwhile, phenol seemed to show the largest deviation from the isotherm even after the humidity correction (see figure 6(a)). In this case, we speculate that there is a co-operative aspect, where there is an additional water mediated phenol adsorption at similar concentrations. Despite these complexities, we would like to conclude, by stressing the importance of understanding these mechanisms. Besides being used for corrective measure, we believe that this will act as an initial step towards the refinements of such biohybrid multi-sensor arrays for in-situ sensitive and selective detection of VOCs.

VOC Discrimination

In this study, phenol and hexanoic acid were chosen for their potential biomedical application. To challenge the selectivity of the biohybrid multi-sensor array, two other VOCs either with similar molecular weight and/or physicochemical properties were chosen. On top of $\Delta RIU(n-1)_{eq}$, the dissociation rate constant k_d, was used in order to test for their potential discriminatory capabilities, (see figure $S8$(b), Supporting Information for parameter extraction information). Since diffusion was often reported as key rate-limiting factor for the association rate constant k_a,[63] it was ignored. On the other hand k_d was dictated by the strength of

short-range interactions, such as Van Der Waals interactions, hydrogen bonds, hydrophobic interactions and electrostatic interactions.[64] Not only was this kinetic parameter unique for each sensor/VOC interaction but it was also independent of the concentration effect making it an ideal descriptor for discriminatory purposes. To correct the concentration-dependence for the steady state response and other drift related variation, a quadratic normalization (see Supporting Information for details) was performed on both descriptors. Moreover, a discernible response contrast was visible only after $\Delta RIU(n-1)_{eq} > 2 \times 10^{-4}$. Therefore, only the last 4 highest VOC concentrations (including the high humidity dose injection), more or less on the linear 'Henry's region' of the isotherm, were considered. Principal component analysis (PCA) was used to visualise the sensor arrays ability to distinguish between the 4 VOCs (see figure 6(c) & (d)). The first two principal components (PCs) for $\Delta RIU(n-1)_{eq}$ seemed to distinguish the 3 VOC doses at near dry conditions. However, for the humidity infused dose there were overlaps, even after the RH corrections, the deviation from the VOC clusters were significant, especially for the most sensitive VOCs: phenol and hexanoic acid. On the other hand, the concentration-independent, kinetic descriptor, k_d showed clear classification of VOCs including the humidity infused dose injection (see figure 6(d)). The grouping of the hexanoic acid humidity dose was of particular interest, as the classification was not affected by the humidity being changed in the middle of the desorption phase (see figure 5(d-i)). This shows that the heterogeneity of these surfaces are of two fold both in terms of surface morphology and physicochemical characteristics.

Finally, A summary of the unique characteristics of this biohybrid e-nose and its performance is compared with an exhaustive list of previously reported e-nose systems, utilizing peptide-immobilized multi-sensor arrays (see table $S3$, Supporting Information). Our system showed superior sensitivities and discriminatory capabilities for an array, with a single sequence, only varying in surface bioarchitecture. We believe, far greater performances can be achieved by increasing the quantity of sensors and their diversity through other SLP sequences. Furthermore, besides the use of data driven analyses (like PCA), with abundant

data, from refined multi-sequence arrays, we would be able to utilize event-driven artificial intelligence techniques.[6] This coupled with deep learning algorithms expands the potential of this novel biomaterial.

Conclusion

In summary, we have developed 'biohybrid' structures that self-assemble onto Au surfaces, using a novel $CG_7{-}NH_2$ SLP sequence, for the detection and discrimination of VOCs. These surfaces were achieved with a two pronged self-assembly process: an initial hierarchical self-assembly phase in solution followed by their sedimentation and subsequent SAMs formation phase surrounding the immobilized hierarchical nanostructures. By manipulating the dynamic structural equilibrium we were able to simply vary solution properties, such as pH, water content and SLP concentration to tune the morphological and physicochemical diversity of the sensing elements. To gauge its potential for the e-nose application, a 5 element sensor array was constructed with one SLP only varying in biohybrid structuration. The sensitivity of sensor array was bench-marked with hexanoic acid and phenol, giving a LOD of < 1 ppbv and 6 ppbv, respectively. Its discriminatory capability was analyzed with both, concentration-dependent ($\Delta RIU(n-1)_{eq}$) and -independent (k_d) descriptors. For the dry VOC dose injections (above a certain threshold) the classification was successful. However, humidity infused doses proved problematic for $\Delta RIU(n-1)_{eq}$, even after the humidity related response change was corrected using BET fitted water vapor adsorption models. Satisfyingly, k_d was identified as a robust classification descriptor for these surfaces.

Ultimately, we strongly believe that this study will act as an initial road map for the development of a novel class of peptide-based, multi-structural, biohybrid surfaces. Having a plethora of other supramolecular nanostructures accessible with peptide self-assembly, the possible amalgamations are vast. Not only would we be able to produce surfaces with quite contrasting morphologies but also manipulate their physicochemical properties by controlling

the regions of the peptide that will have molecular accessibility. Therefore, beyond its e-nose application, we anticipate the potential of these biohybrid surfaces to be far reaching, especially in the field of biosensing.

Materials and Methods

Materials

All chemicals were of analytical grade and used as received without any further purification. The designer SLP $CG_7{-}NH_2$ was purchased from SB-PEPTIDE. Its ESI-MS spectrum can be found in figure $S1$, Supporting Information. DMSO ($\geq$ 99.9 %) and the tested VOCs: Phenol ($\geq$ 99 %), 1-Hexanol (98 %), Butyric Acid ($\geq$ 99 %) and Hexanoic acid ($\geq$ 99 %) were purchased from Sigma-Aldrich. All chemicals were handled under a fume-hood. No other significant risk was associated with this work.

SPRI prism fabrication

Metal film deposition on the active prism surface was performed using an electron (e-)beam evaporator, $MEB550-S$ (Plassys), in a clean-room environment. Initially, 25 mm right apex angled $N-BK7^{®}$ glass prism (Edmund optics) was etched with an Ar^+ ion gun at 250 V. With an etch rate of $\sim$ 5 nm/min for 24 s to ensure an increased flattening of the prism surface before deposition. Furthermore, the etching was done at a inclined angle of 20° with an ion flux. For homogeneous exposure to the ion flux, the sample was rotated clock-wise and counter-clockwise at 12 s intervals. Firstly a 2 nm Cr adhesive layer was deposited at 0.1 nm/s followed by 53 nm of Au at 0.25 nm/s (Cr/Au configuration was previously optimised for higher sensitivity, stability and dynamic range[15,65]). The pressure of the sample chamber during deposition was maintained at $\sim 5 \times 10^{-8}$ mbar, in-line with the gold standard of ultra high vacuum deposition ($< 10^{-7}$ torr[66]).

Sensor Array Preparation

Sensor arrays were simultaneously immobilized on a flat $D\,263^{®}$ glass slide treated with Cr/Au - 1.5 ± 0.5 nm/55 ± 3 nm metal layers (Schott) and the fabricated SPRI prism. Initially, both samples were subjected to a plasma cleaning process. A low pressure FEMTO plasma generator (Diener electronics), with 75 % vol. O_2 and 25 % vol. Ar at 0.6 mbar was used to generate the plasma at 80 W. The cleaning was carried out for 3 mins. To reduce the hydrophilicity of the cleaned Au surface the samples were placed in a sealed environment for 48 hours. An automated, non-contact, inkjet-based spotting robot, sciFLEXARRAYER (Scienion) was used for arraying. 5 spotting solutions ($DW65$, $DW35$, $DMSO$, $DW65H$ and $DW65L$), each with 3 different SLP concentrations (0.01 mM, 0.1 mM and 0.5 mM) were spotted as 5 nL droplets on the prism. The water content and pH of each spotting solution are detailed in figure 3(a-ii). The $DW65H$ and $DW65L$ spotting solutions were adjusted to $pH = 11.5$ and $pH = 2$ by using HCl and NaOH, respectively. The pH of all solutions was measured using an electronic pH meter Basic 20 (Crison instruments). 3 replicates of the 15 conditions were randomly spotted to avoid any positional biases on the SPRI sensor chip. Simultaneously, larger 0.5 μL drops were spotted on the Au-coated glass slide for easier identification of the spots during AFM surface characterization. Then, the SPRI sensor chip and spotted glass slide were placed, at 25°C, in a salt saturated, humidity-controlled chamber (94 % RH[67]) for 18 hours. Following which, both samples were rinsed with milli-Q water and dried using Ar gas. Finally, they were stored at 4°C prior to characterization and gas-phase sensing.

SPRI Set-up

A custom-built SPRI set-up was utilised in this study (see figure $S9$(a), Supporting Information).[13–15,65] The setup was placed in a temperature controlled oven (Memmert) and the incident beam was guided into the setup using a 200 μm optical fiber. A working wavelength $\lambda_w = 632.8$ nm was achieved using a 625 nm intensity modulated $M625F2$ LED (Thorlabs) set to 166 mA, and a $FL05632.8-3$ bandpass filter with central wavelength 632.8 nm and bandwidth 3 nm, (Thorlabs). To achieve Transverse Magnetic/Electric (TM/TE) modes $LPVISE100-A$ linear polarizer (Thorlabs) with extinction ratio $> 1000:1$ was used. The incident beam was initially diffused and then collimated using an achromatic aspheric glass lens (Edmund Optics). The reflected light was guided by an additional lens system and a 16−bit AVT PIKE $F-145B$ CCD camera (Allied Vision Technologies) captured the images at 1280×960 pixel resolution with a pixel size of 8.3 μm. The sensors were defined as circles having a 350 μm diameter at the center of the spot. For temporal reflectivity measurements, initially, the most suitable θ_w was identified via angular scans at increments of 0.125°. At θ_w the images were continuously recorded at a frame capture rate of 30 fps, in 8−bit monochrome color. Using a custom LabVIEW platform the reflectivity was evaluated. The reflectivity measures were then converted to refractive index unit ($RIU(n-1)$) using the evaluated $\partial R/\partial n$ for each sensing element[15] (see Supporting Information for details).

Gas-phase Fluidic Set-up

Air was used as the carrier gas and generated using a Zero Gas system (Umwelttechnik MCZ). Ambient air was compressed (3 bar) and subsequently cleaned with catalytic filters (< 1 ppmv of CO_2+CO) and further dried with a charcoal column ($\sim 2\,\%$ RH). Initially, the dry air was passed through the humidity region where humidity could be introduced to it in the Wet line or, alternatively, was bypassed via the Dry line. To control the humidity levels the Wet and Dry line were mixed using mass flow controllers (Bronkhorst). The total flow

was maintained at 250 mL/min. The pressure in this region was maintained using a pressure controller (Bronkhorst) at $\sim$ 1500 mbar. Secondly, the carrier gas entered the VOC region where the VOC was introduced. Similarly, this region composed of two lines: the purge line (only carrying clean carrier gas) and the VOC line. Each line had the ability to be alternated, independently, or mixed to further dilute the VOCs being analysed. The total flow rate in this region was maintained at 100 mL/min with an additional pressure controller. The baseline pressure was set to 50 mbar above ambient conditions (absolute pressure of 1063.25 mbar) to ensure carrier gas flow through the analysis chamber, which was hermetically sealed with a volume $\sim 470\,\mathrm{mm}^3$. The pressure controller was able to precisely control the pressure within the chamber to perform pressure-based calibrations[68] and subsequent $\partial R/\partial n$ calculations.[15] All the tubes were composed of PTFE to minimise water and VOC adsorption. Stainless steel connectors, valves and additional tube connectors enabled the integration of all components while minimising these anti-fouling properties throughout the entire system (see figure $S9$(b), Supporting Information).

Dynamic Headspace (DHS) Generation

Unlike in liquid media, controlled evaporation techniques need to be adopted when generating reproducible gaseous 'Headspaces'. To humidify the carrier gas, the volume evaporation technique was followed using a high pressure bubbler (Swageloke) attached to the Wet line. $HIH6100$ temperature and humidity sensor (Honeywell) coupled to an Arduino® board (Arduino) was utilised to continuously monitor and record the temperature and humidity of the DHS, immediately after the analysis chamber. To introduce VOC into the carrier gas the surface evaporation technique was used. $200 - 300\,\mu$L of liquid/ 50 mg of solid VOC was dissolved in 4 mL of mineral oil (Sigma Aldrich) in hermetically sealed container on the VOC line. For $\sim$ 2 mins the mixture was continuously agitated, during which time the carrier gas was flown over it. The mineral oil acted as a matrix for the dissolved VOCs

where the evaporation was controlled and rapidly equilibrated regardless of the volatility of the compound.[69] Once equilibrated, the DHS was used in 5 mins dose injections and purged for 5 mins with clean carrier gas. For the different VOC concentration ramps, the first 5 dose injections and subsequent purges were tested at $0-2\,\%$ RH and the final dose injection and purge was tested at $\sim 35\,\%$ RH. For the hexanoic acid ramp the RH was cut off during the dissociation phase. A ppbRAE300 PID (RAE Systems) was used to continuously record the concentration of the VOC in the DHS (detection limit 1 ppbv) .

Transmission Electron Microscopy

The SLP solutions were freshly prepared $4-5$ hours prior to TEM analysis. To understand the time evolution of these nanostructures, the solutions were re-analysed after 3 days. Images were acquired on a Tecnai $F20$ microscope (ThermoFisher) at 200 kV on a $4K \times 4K$ resolution Ceta camera. The specimen was prepared by sonicating the spotting solution for 10 mins and depositing it on a grid covered by a homemade carbon film. A carbon film with nominal thickness of 1 nm was evaporated onto a freshly cleaved mica surface. The carbon film was then floated off the mica in water and retrieved by a 300 mesh Cu electron microscopy grid. Around $4\,\mu$L of sample was deposited onto the grid with the carbon film. The liquid was left on the copper grid for about 10 s and then blotted with a filter paper and dried in air before imaging. The images were contrast corrected using the Fiji software.[70]

Atomic Force Microscopy

For surface characterization the scans were performed on the spotted Au-coated glass slide using a Dimension Icon (Bruker). All scans were done using $SAA-HPI-SS$ (Bruker) high resolution tips with a Si_3N_4 cantilever having a spring constant 0.25 N/m and a 'super sharp' integral tip with a diameter of 2 nm. Scans were performed using ScanAsyst®, a type

of PeakForce tapping mode®. For the 0.1 mM SLP spots, an area of $1 \times 1\,\mu m^2$ and $2 \times 2\,\mu m^2$ were scanned at 1024×1024 and 512×512 pixel resolutions, respectively. For the other SLP spots (0.01 mM and 0.5 mM) an area of $1 \times 1\,\mu m^2$ were scanned at a 512×512 pixel resolution. All images were leveled and analysed using Gwyddion and its built-in algorithms.

Acknowledgement

The authors thank the following organizations for funding the PhD scholarship of J.S.W. (Fondation Nanosciences), of M.E.K (ANR and Labex LANEF du Programme d'Investissements d'Avenir: ANR-10-LABX-51-01), and of E.J. (CEA). The work was carried out at the SyMMES laboratory, supported as part of Labex LANEF and Labex ARCANE. We thank Dr. Guy Schoehn for his support. This work used the platforms of the Grenoble Instruct-ERIC center (ISBG; UAR 3518 CNRS-CEA-UGA-EMBL) within the Grenoble Partnership for Structural Biology (PSB), supported by FRISBI (ANR-10-INBS-0005-02) and GRAL, financed within the Université Grenoble Alpes graduate school (Ecoles Universitaires de Recherche) CBH-EUR-GS (ANR-17-EURE-0003). The electron microscope facility is supported by the Auvergne-Rhône-Alpes Region, the Fondation Recherche Medicale (FRM), the fonds FEDER and the GIS-Infrastructures en Biologie Sante et Agronomie (IBiSA). IBS acknowledges integration into the Interdisciplinary Research Institute of Grenoble (IRIG, CEA).

Supporting Information Available

Additional results: ESI-MS spectrum For $CG_7{-}NH_2$, TEM Images of fiber meshes and agglomerates, AFM scan of biohybrid spot boundary, Au grain size characterization, Gaussian mixture model, additional AFM images and concentration effects, Bulk refractive index sensitivity characterisation: pre- and post- usage, Response descriptor extraction, Freundlich

and BET isotherms and fitted parameters, Comparison of our biohybrid e-nose with an exhaustive list of significant e-nose systems, PCA evaluation, custom built SPRI and gas-phase fluid schematic.

Click to view the supporting information

References

(1) Persaud, K.; Dodd, G. Analysis of discrimination mechanisms in the mammalian olfactory system using a model nose. *Nature* **1982**, *299*, 352–355.

(2) Gardner, J. W.; Bartlett, P. N. A brief history of electronic noses. *Sens. Actuators, B* **1994**, *18*, 210–211.

(3) Maho, P.; Herrier, C.; Livache, T.; Rolland, G.; Comon, P.; Barthelmé, S. Reliable chiral recognition with an optoelectronic nose. *Biosens. Bioelectron.* **2020**, *159*, 112183.

(4) Park, S. Y.; Kim, Y.; Kim, T.; Eom, T. H.; Kim, S. Y.; Jang, H. W. Chemoresistive materials for electronic nose: Progress, perspectives, and challenges. *InfoMat* **2019**, *1*, 289–316.

(5) Hu, W.; Wan, L.; Jian, Y.; Ren, C.; Jin, K.; Su, X.; Bai, X.; Haick, H.; Yao, M.; Wu, W. Electronic Noses: From Advanced Materials to Sensors Aided with Data Processing. *Adv. Mater. Technol.* **2019**, *4*, 1800488.

(6) Jeong, S.-Y.; Kim, J.-S.; Lee, J.-H. Rational Design of Semiconductor-Based Chemiresistors and their Libraries for Next-Generation Artificial Olfaction. *Adv. Mater.* **2020**, *32*, 2002075.

(7) Chen, J.; Chen, Z.; Boussaid, F.; Zhang, D.; Pan, X.; Zhao, H.; Bermak, A.; Tsui, C.-Y.; Wang, X.; Fan, Z. Ultra-Low-Power Smart Electronic Nose System Based on Three-Dimensional Tin Oxide Nanotube Arrays. *ACS Nano* **2018**, *12*, 6079–6088.

(8) Kang, H.; Cho, S.-Y.; Ryu, J.; Choi, J.; Ahn, H.; Joo, H.; Jung, H.-T. Multiarray Nanopattern Electronic Nose (E-Nose) by High-Resolution Top-Down Nanolithography. *Adv. Funct. Mater.* **2020**, *30*, 2002486.

(9) Tan, W. C.; Ang, K.-W. Volatile Organic Compound Sensors Based on 2D Materials. *Adv. Electron. Mater.* **2021**, *7*, 2001071.

(10) Bag, A.; Lee, N.-E. Gas sensing with heterostructures based on two-dimensional nanostructured materials: a review. *J. Mater. Chem. C* **2019**, *7*, 13367–13383.

(11) Chen, Z.; Wang, J.; Pan, D.; Wang, Y.; Noetzel, R.; Li, H.; Xie, P.; Pei, W.; Umar, A.; Jiang, L.; Li, N.; Rooij, N. F. d.; Zhou, G. Mimicking a Dog's Nose: Scrolling Graphene Nanosheets. *ACS Nano* **2018**, *12*, 2521–2530.

(12) Mendes, A. C.; Baran, E. T.; Reis, R. L.; Azevedo, H. S. Self-assembly in nature: using the principles of nature to create complex nanobiomaterials. *Wiley Interdiscip. Rev.: Nanomed. Nanobiotechnol.* **2013**, *5*, 582–612.

(13) Brenet, S.; John-Herpin, A.; Gallat, F.-X.; Musnier, B.; Buhot, A.; Herrier, C.; Rousselle, T.; Livache, T.; Hou, Y. Highly-Selective Optoelectronic Nose Based on Surface Plasmon Resonance Imaging for Sensing Volatile Organic Compounds. *Anal. Chem.* **2018**, *90*, 9879–9887.

(14) Brenet, S.; Weerakkody, J. S.; Buhot, A.; Gallat, F.-X.; Mathey, R.; Leroy, L.; Livache, T.; Herrier, C.; Hou, Y. Improvement of sensitivity of surface plasmon resonance imaging for the gas-phase detection of volatile organic compounds. *Talanta* **2020**, *212*, 120777.

(15) Weerakkody, J. S.; Brenet, S.; Livache, T.; Herrier, C.; Hou, Y.; Buhot, A. Optical Index Prism Sensitivity of Surface Plasmon Resonance Imaging in Gas Phase: Experiment versus Theory. *J. Phys. Chem. C* **2020**, *124*, 3756–3767.

(16) Aryballe. `https://aryballe.com/`.

(17) Zhang, S.; Holmes, T.; Lockshin, C.; Rich, A. Spontaneous assembly of a self-complementary oligopeptide to form a stable macroscopic membrane. *Proc. Natl. Acad. Sci. U. S. A.* **1993**, *90*, 3334–3338.

(18) Qiu, F.; Chen, Y.; Zhao, X. Comparative studies on the self-assembling behaviors of cationic and catanionic surfactant-like peptides. *J. Colloid Interface Sci.* **2009**, *336*, 477–484.

(19) Fatouros, D. G.; Lamprou, D. A.; Urquhart, A. J.; Yannopoulos, S. N.; Vizirianakis, I. S.; Zhang, S.; Koutsopoulos, S. Lipid-like Self-Assembling Peptide Nanovesicles for Drug Delivery. *ACS Appl. Mater. Interfaces* **2014**, *6*, 8184–8189.

(20) Stendahl, J. C.; Rao, M. S.; Guler, M. O.; Stupp, S. I. Intermolecular Forces in the Self-Assembly of Peptide Amphiphile Nanofibers. *Adv. Funct. Mater.* **2006**, *16*, 499–508.

(21) Li, J.; Wang, J.; Zhao, Y.; Zhou, P.; Carter, J.; Li, Z.; Waigh, T. A.; Lu, J. R.; Xu, H. Surfactant-like peptides: From molecular design to controllable self-assembly with applications. *Coord. Chem. Rev.* **2020**, *421*, 213418.

(22) Nagai, A.; Nagai, Y.; Qu, H.; Zhang, S. Dynamic Behaviors of Lipid-Like Self-Assembling Peptide A6D and A6K Nanotubes. *J. Nanosci. Nanotechnol.* **2007**, *7*, 2246–2252.

(23) Khoe, U.; Yang, Y.; Zhang, S. Self-Assembly of Nanodonut Structure from a Cone-Shaped Designer Lipid-like Peptide Surfactant. *Langmuir* **2009**, *25*, 4111–4114.

(24) von Maltzahn, G.; Vauthey, S.; Santoso, S.; Zhang, S. Positively Charged Surfactant-like Peptides Self-assemble into Nanostructures. *Langmuir* **2003**, *19*, 4332–4337.

(25) Vauthey, S.; Santoso, S.; Gong, H.; Watson, N.; Zhang, S. Molecular self-assembly of surfactant-like peptides to form nanotubes and nanovesicles. *Proc. Natl. Acad. Sci. U. S. A.* **2002**, *99*, 5355–5360.

(26) Santoso, S.; Hwang, W.; Hartman, H.; Zhang, S. Self-assembly of Surfactant-like Pep-

tides with Variable Glycine Tails to Form Nanotubes and Nanovesicles. *Nano Lett.* **2002**, *2*, 687–691.

(27) Chen, Y.; Tang, C.; Xing, Z.; Zhang, J.; Qiu, F. Ethanol induced the formation of -sheet and amyloid-like fibrils by surfactant-like peptide A6K. *J. Pept. Sci.* **2013**, *19*, 708–716.

(28) Bai, J.; Chen, C.; Wang, J.; Zhang, Y.; Cox, H.; Zhang, J.; Wang, Y.; Penny, J.; Waigh, T.; Lu, J. R.; Xu, H. Enzymatic Regulation of Self-Assembling Peptide A9K2 Nanostructures and Hydrogelation with Highly Selective Antibacterial Activities. *ACS Appl. Mater. Interfaces* **2016**, *8*, 15093–15102.

(29) Pouget, E.; Dujardin, E.; Cavalier, A.; Moreac, A.; Valéry, C.; Marchi-Artzner, V.; Weiss, T.; Renault, A.; Paternostre, M.; Artzner, F. Hierarchical architectures by synergy between dynamical template self-assembly and biomineralization. *Nat. Mater.* **2007**, *6*, 434–439.

(30) Wang, X.; Corin, K.; Baaske, P.; Wienken, C. J.; Jerabek-Willemsen, M.; Duhr, S.; Braun, D.; Zhang, S. Peptide surfactants for cell-free production of functional G protein-coupled receptors. *Proc. Natl. Acad. Sci. U. S. A.* **2011**, *108*, 9049–9054.

(31) Loo, Y.; Lakshmanan, A.; Ni, M.; Toh, L. L.; Wang, S.; Hauser, C. A. E. Peptide Bioink: Self-Assembling Nanofibrous Scaffolds for Three-Dimensional Organotypic Cultures. **2015**, *15*, 6919–6925.

(32) Carlini, A. S.; Choi, W.; McCallum, N. C.; Gianneschi, N. C. pH-Responsive Charge-Conversion Progelator Peptides. *Adv. Funct. Mater.* **2021**, *31*, 2007733.

(33) Baker, N. A.; Sept, D.; Joseph, S.; Holst, M. J.; McCammon, J. A. Electrostatics of nanosystems: Application to microtubules and the ribosome. *Proc. Natl. Acad. Sci. U. S. A.* **2001**, *98*, 10037–10041.

(34) Dolinsky, T. J.; Czodrowski, P.; Li, H.; Nielsen, J. E.; Jensen, J. H.; Klebe, G.; Baker, N. A. PDB2PQR: expanding and upgrading automated preparation of biomolecular structures for molecular simulations. *Nucleic Acids Res.* **2007**, *35*, W522–W525.

(35) Han, S.; Xu, W.; Meiwen, C.; Jiqian, W.; Xia, D.; Xu, H.; Zhao, X.; R. Lu, J. Interfacial adsorption of cationic peptide amphiphiles : a combined study of in situ spectroscopic ellipsometry and liquid AFM. *Soft Matter* **2012**, *8*, 645–652.

(36) Yamamoto, M.; Matsumae, T.; Kurashima, Y.; Takagi, H.; Suga, T.; Itoh, T.; Higurashi, E. Comparison of Argon and Oxygen Plasma Treatments for Ambient Room-Temperature Wafer-Scale Au–Au Bonding Using Ultrathin Au Films. *Micromachines* **2019**, *10*, 119.

(37) Xu, H.; Wang, J.; Han, S.; Wang, J.; Yu, D.; Zhang, H.; Xia, D.; Zhao, X.; Waigh, T. A.; Lu, J. R. Hydrophobic-Region-Induced Transitions in Self-Assembled Peptide Nanostructures. *Langmuir* **2009**, *25*, 4115–4123.

(38) Yang, L.-J.; Yang, X.-Q.; Huang, K.-M.; Jia, G.-Z.; Shang, H. Dielectric Properties of Binary Solvent Mixtures of Dimethyl Sulfoxide with Water. *Int. J. Mol. Sci.* **2009**, *10*, 1261–1270.

(39) Levin, A.; Hakala, T. A.; Schnaider, L.; Bernardes, G. J. L.; Gazit, E.; Knowles, T. P. J. Biomimetic peptide self-assembly for functional materials. *Nat. Rev. Chem.* **2020**, *4*, 615–634.

(40) Moyer, T. J.; Kassam, H. A.; Bahnson, E. S. M.; Morgan, C. E.; Tantakitti, F.; Chew, T. L.; Kibbe, M. R.; Stupp, S. I. Shape-Dependent Targeting of Injured Blood Vessels by Peptide Amphiphile Supramolecular Nanostructures. *Small* **2015**, *11*, 2750–2755.

(41) Wang, J.; Han, S.; Meng, G.; Xu, H.; Xia, D.; Zhao, X.; Schweins, R.; Lu, J. R.

Dynamic self-assembly of surfactant-like peptides A6K and A9K. *Soft Matter* **2009**, *5*, 3870–3878.

(42) Knowles, T. P. J.; Waudby, C. A.; Devlin, G. L.; Cohen, S. I. A.; Aguzzi, A.; Vendruscolo, M.; Terentjev, E. M.; Welland, M. E.; Dobson, C. M. An Analytical Solution to the Kinetics of Breakable Filament Assembly. *Science* **2009**, *326*, 1533–1537.

(43) Serem, W. K.; Bett, C. K.; Ngunjiri, J. N.; Garno, J. C. Studies of the growth, evolution, and self-aggregation of -amyloid fibrils using tapping-mode atomic force microscopy. *Microsc. Res. Tech.* **2011**, *74*, 699–708.

(44) Dujardin, A.; Wolf, P. D.; Lafont, F.; Dupres, V. Automated multi-sample acquisition and analysis using atomic force microscopy for biomedical applications. *PLoS One* **2019**, *14*, e0213853.

(45) Colherinhas, G.; Fileti, E. Molecular Dynamics Study of Surfactant-Like Peptide Based Nanostructures. *J. Phys. Chem. B* **2014**, *118*, 12215–12222.

(46) Eichstaedt, K.; Szpotkowski, K.; Grajda, M.; Gilski, M.; Wosicki, S.; Jaskólski, M.; Szumna, A. Self-Assembly and Ordering of Peptide-Based Cavitands in Water and DMSO: The Power of Hydrophobic Effects Combined with Neutral Hydrogen Bonds. *Chem. - Eur. J.* **2019**, *25*, 3091–3097.

(47) Wang, J.; Yuan, C.; Han, Y.; Wang, Y.; Liu, X.; Zhang, S.; Yan, X. Trace Water as Prominent Factor to Induce Peptide Self-Assembly: Dynamic Evolution and Governing Interactions in Ionic Liquids. *Small* **2017**, *13*, 1702175.

(48) Deshmukh, S. A.; Solomon, L. A.; Kamath, G.; Fry, H. C.; Sankaranarayanan, S. K. R. S. Water ordering controls the dynamic equilibrium of micelle–fibre formation in self-assembly of peptide amphiphiles. *Nat. Commun.* **2016**, *7*, 12367.

(49) Di Gioacchino, M.; Ricci, M. A.; Imberti, S.; Holzmann, N.; Bruni, F. Hydration and aggregation of a simple amino acid: The case of glycine. *J. Mol. Liq.* **2020**, *301*, 112407.

(50) Dighe, A. V.; Singh, M. R. Solvent fluctuations in the solvation shell determine the activation barrier for crystal growth rates. *Proc. Natl. Acad. Sci. U. S. A.* **2019**, *116*, 23954–23959.

(51) Parsa, M. M.; Harmand, S.; Sefiane, K. Mechanisms of pattern formation from dried sessile drops. *Adv. Colloid Interface Sci.* **2018**, *254*, 22–47.

(52) Xu, W.; Leeladhar, R.; Kang, Y. T.; Choi, C.-H. Evaporation Kinetics of Sessile Water Droplets on Micropillared Superhydrophobic Surfaces. *Langmuir* **2013**, *29*, 6032–6041.

(53) Li, P.; Li, Y.; Zhou, Z.-K.; Tang, S.; Yu, X.-F.; Xiao, S.; Wu, Z.; Xiao, Q.; Zhao, Y.; Wang, H.; Chu, P. K. Evaporative Self-Assembly of Gold Nanorods into Macroscopic 3D Plasmonic Superlattice Arrays. *Adv. Mater.* **2016**, *28*, 2511–2517.

(54) Cote, Y.; Fu, I. W.; Dobson, E. T.; Goldberger, J. E.; Nguyen, H. D.; Shen, J. K. Mechanism of the pH-Controlled Self-Assembly of Nanofibers from Peptide Amphiphiles. *J. Phys. Chem. C* **2014**, *118*, 16272–16278.

(55) Poole, L. B. The Basics of Thiols and Cysteines in Redox Biology and Chemistry. *Free radical biology & medicine* **2015**, *0*, 148–157.

(56) Kumar, S.; Huang, J.; Abbassi-Ghadi, N.; Španěl, P.; Smith, D.; Hanna, G. B. Selected Ion Flow Tube Mass Spectrometry Analysis of Exhaled Breath for Volatile Organic Compound Profiling of Esophago-Gastric Cancer. *Anal. Chem.* **2013**, *85*, 6121–6128.

(57) Walsh, K.; Mayer, S.; Rehmann, D.; Hofmann, T.; Glas, K. Equilibrium data and its analysis with the Freundlich model in the adsorption of arsenic(V) on granular ferric hydroxide. *Sep. Purif. Technol.* **2020**, *243*, 116704.

(58) Güntner, A. T.; Koren, V.; Chikkadi, K.; Righettoni, M.; Pratsinis, S. E. E-Nose Sensing of Low-ppb Formaldehyde in Gas Mixtures at High Relative Humidity for Breath Screening of Lung Cancer? *ACS Sens.* **2016**, *1*, 528–535.

(59) Teng, C. D.; Zarrintan, M. H.; Groves, M. J. Water Vapor Adsorption and Desorption Isotherms of Biologically Active Proteins. *Pharm. Res.* **1991**, *8*, 191–195.

(60) Zhou, X.; Zhang, J.; Jiang, T.; Wang, X.; Zhu, Z. Humidity detection by nanostructured ZnO: A wireless quartz crystal microbalance investigation. *Sens. Actuators, A* **2007**, *135*, 209–214.

(61) Chang, Y.; Tang, N.; Qu, H.; Liu, J.; Zhang, D.; Zhang, H.; Pang, W.; Duan, X. Detection of Volatile Organic Compounds by Self-assembled Monolayer Coated Sensor Array with Concentration-independent Fingerprints. *Sci. Rep.* **2016**, *6*, 23970.

(62) Mel'gunov, M. S.; Ayupov, A. B. Direct method for evaluation of BET adsorbed monolayer capacity. *Microporous Mesoporous Mater.* **2017**, *243*, 147–153.

(63) Pan, C. Measuring Dissociation Rate Constants of Protein Complexes through Subunit Exchange: Experimental Design and Theoretical Modeling. *PLoS One* **2011**, *6*, e28827.

(64) Selzer, T.; Albeck, S.; Schreiber, G. Rational design of faster associating and tighter binding protein complexes. *Nat. Struct. Biol.* **2000**, *7*, 537–541.

(65) Weerakkody, J. S.; Hurot, C.; Brenet, S.; Mathey, R.; Herrier, C.; Livache, T.; Buhot, A.; Hou, Y. Surface plasmon resonance imaging-based optoelectronic nose: fundamental study on the effects of temperature and humidity. Optical Sensing and Detection VI. 2020; p 1135414.

(66) McPeak, K. M.; Jayanti, S. V.; Kress, S. J. P.; Meyer, S.; Iotti, S.; Rossinelli, A.; Norris, D. J. Plasmonic Films Can Easily Be Better: Rules and Recipes. *ACS Photonics* **2015**, *2*, 326–333.

(67) Greenspan, L. Humidity fixed points of binary saturated aqueous solutions. *J. Res. Natl. Bur. Stand., Sect. A* **1977**, *81A*, 89.

(68) Herrier, C.; Hou-Broutin, Y.; Gallat, F.-X.; Livache, T.; Rousselle (CEA, CNRS, UGA, Aryballe Technologies), T. Fra. 2018158458. patent WO2018158458A1, 2018.

(69) Liu, Z.; Wene, M. J. Measurement of Gas–Liquid Partition Coefficient and Headspace Concentration Profiles of Perfume Materials by Solid-Phase Microextraction and Capillary Gas Chromatography–Mass Spectrometry. *J. Chromatogr. Sci.* **2000**, *38*, 377–382.

(70) Schindelin, J. et al. Fiji: an open-source platform for biological-image analysis. *Nat. Methods* **2012**, *9*, 676–682.

TOC Graphic

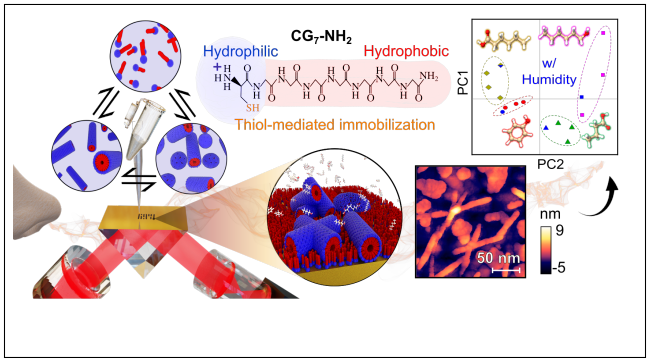
CG7-NH2
Hydrophilic
Hydrophobic
Thiol-mediated immobilization
PC1
PC2
w/
Humidity
nm
9
-5
50 nm